Measurement of Physical Conditions in Stellar Jets

Patrick Hartigan[1]

Department of Physics and Astronomy, Rice University, Houston TX 77005-1892 USA hartigan@sparky.rice.edu

This article summarizes the physics needed to interpret spectra of stellar jets, reviews the history of analysis techniques applied to these objects, discusses some recent results, and considers the prospects for future research in this area.

1 Introduction

Over fifty years have passed since Herbig [26] first published spectra of two bright nebulous emission line sources located in the star formation region NGC 1999. The objects, which we now know as the prototype Herbig-Haro objects HH 1 and HH 2, had also appeared as emission line sources in an Hα prism survey of the region by Haro [15]. Unlike other emission line nebulae known at the time (such as H II regions), no blue stars existed nearby that might ionize these nebulae. Moreover, as Herbig noted in his paper, the emission-line spectra were quite peculiar: forbidden emission lines from low ionization species such as [S II] and [O I] were unusually strong, and yet high ionization lines of [O III] and [Ne III] were also present.

In the years that followed Herbig's paper, Herbig-Haro (HH) objects have played an increasingly pivotal role in clarifying how stars form. We now know that HH objects represent regions of shocked gas in collimated supersonic jets that emerge along the rotation axes of accretion disks. The existence of supersonic outflowing gas from a source where material is supposed to be accreting onto the central object is at first glance quite surprising, and the ubiquity of the phenomenon suggests that jets are an essential aspect of the star formation process. Because jets are spatially resolved and show clear proper motions, emission-line images immediately reveal something about the kinematics of the flows, which in turn helps to constrain models of jets and accretion disks.

However, if we wish to understand the internal dynamics of jets and obtain a deeper appreciation of how these flows connect with their disks, we

must consider the processes that heat the jet, and we must measure physical conditions along the outflow, such as the temperature, density, ionization fraction, magnetic fields, and internal velocities. In many ways, HH objects are particularly well-suited for such analyses because they emit at least a dozen bright emission lines, all of which are optically thin. Hence, the emitted light escapes freely and there are no complex radiative transfer issues to consider as there are, for example, in emission line spectra of accretion disks around young stars.

This review consists of three parts. In the next section I summarize the basic atomic physics that underlies the analysis of emission lines in stellar jets. The techniques are similar to those employed to study other emission nebulae such as H II regions and planetary nebulae, but the relatively low ionization, high densities, and inhomogeneous conditions present behind shock waves in jets pose some unique challenges in the interpretation of the data. In Sect. 3, I present an overview of the history of the analysis of line ratios in HH objects. Extracting physical information from the spectra of HH objects began soon after their discovery and continues to this day, with analysis methods steadily improving. There is a great deal to learn about how science is done by understanding how the incremental advances from different groups have contributed to our present knowledge. In Sect. 4, I review some new results just accepted for publication that deal with magnetic field strengths along jets, and with heating and cooling within 100 AU of the source.

2 Atomic Physics of Stellar Jets

2.1 Observations of Electron Temperature and Electron Density

Connection of Observed Line Fluxes with Level Populations in Atoms

Before we consider the physical processes at work in stellar jets, we should first have some idea as to what we actually observe when we see emission lines from an extended object. Emission lines in stellar jets occur because an atom transitions from an excited bound state to a lower energy bound state. When we speak of an atom in an excited state we really mean that a bound electron in that atom is in a level above the ground state. The atom may come to the excited state in many ways. For example, if the atom is initially in its ground state, a free electron can collide with it and in the process transfer some of the kinetic energy of the collision to the bound electron within the atom, raising the atom to an excited state. Alternatively, if the atom was already in a higher excited state, the collision may de-excite the atom to a lower excited state. Other processes may also leave the atom in an excited state, such as absorbing a photon when the atom is in a lower state, recombining from a higher ionization state, or even as a consequence of charge exchange with another atom.

Regardless of the physical process that leaves the atom in the excited state, if we know the density of atoms in that state we can calculate the amount of light that emerges from a volume of such atoms. In what follows let us define level 1 as the lower level, and level 2 as the upper level. Let n_1 and n_2 refer to the number density of atoms (cm^{-3}) in levels 1 and 2, respectively. Then for a parcel of gas with a number density n_2, the rate of photons emitted from a 1 cm^3 volume is simply $n_2 A_{21}$, where A_{21} is the Einstein A-coefficient for the transition (units s^{-1}). Hence, if we define the volume emission coefficient of the transition j_{21} to be the energy per unit volume, per second, per steradian in the emission line coming from the gas, then

$$j_{21} = \frac{n_2 A_{21} h\nu_{21}}{4\pi} \tag{1}$$

where the units on j_{21} are $\mathrm{erg\,cm^{-3}s^{-1}str^{-1}}$.

The general equation of radiative transfer is

$$\frac{dI}{dl} = -\kappa I + j, \tag{2}$$

where I is the intensity, dl the path length along the line of sight, κ the opacity and j the volume emission coefficient. Equation 2 is basically a definition of what one means by a volume emission coefficient and opacity. Because the densities are low enough in stellar jets that the gas is transparent (optically thin), we can take κ equal to zero. Hence, to obtain the intensity of the emission line we simply integrate the volume emission coefficient along the line of sight,

$$I_{21} = \int j_{21} dl. \tag{3}$$

Intensities are independent of distance to the observer. Hence, at the telescope, if a pixel on a CCD subtends a solid angle Ω, then the rate R_{21} of emission line photons stored per second as electrons on the CCD is given by

$$R_{21} = \frac{I_{21}}{h\nu} \Omega A f, \tag{4}$$

where A is the area of the telescope's aperture, and f is an efficiency factor that takes into account light losses in the Earth's atmosphere, telescope optics and detector. Hence, from an observational point of view, the critical parameter is the number density n_2 of atoms in the upper state. Emission-line ratios are even simpler, and depend only on the relative populations of the upper levels responsible for each line, and on the ratio of the Einstein A-values. Once we determine n_2 for all levels of interest, the connection to the observations is immediate and the analysis is done.

Statistical Equilibrium

A key realization in the analysis of line emission is that the level populations of atoms in a parcel of gas are in statistical equilibrium, that is, that the rate that these levels are populated equals the rate that they are depopulated. There is a distinct difference between statistical equilibrium and local thermodynamic equilibrium (LTE). In LTE, the levels are populated according to the Boltzmann equation

$$\frac{n_2}{n_1} = \frac{g_2}{g_1} e^{-h\nu_{12}/kT}, \tag{5}$$

whereas in statistical equilibrium, low density gases like those found in stellar jets and in the interstellar medium are mostly in the ground state.

Balancing the rates in and out of the upper state for a 2-level atom where collisional excitation, de-excitation, and radiative decay are the dominant processes, we have

$$n_1 n_e C_{12} = n_2 A_{21} + n_2 n_e C_{21}, \tag{6}$$

where n_e is the electron density, and C_{12} and C_{21} are the rate coefficients for collisional excitation and de-excitation, respectively. Units on rate coefficients are $\mathrm{cm}^3\mathrm{s}^{-1}$. Whenever particles of type A interact with those of type B, the rate of the reaction per unit volume is simply $\mathrm{n}_A\mathrm{n}_B\mathrm{C}_{AB}$ $\mathrm{cm}^{-3}\mathrm{s}^{-1}$. For the simple case where A are point-like particles fixed in space and B are particles that move in one direction with a velocity v and cross section σ, $\mathrm{C}_{AB} = \sigma\mathrm{v}$. Thus, it is helpful to think of a rate coefficient as simply the product of a cross-sectional area and an impact velocity. If we know how the cross-section varies with velocity, then it is possible to integrate over arbitrary velocity distributions such as occur in a thermal gas to obtain an average rate coefficient for the reaction.

We can define a critical density n_C to be when the two terms on the right hand side of equation 6 are equal

$$n_C = A_{21}/C_{21}. \tag{7}$$

Notice that the critical density refers to the number density of electrons, not to the number density of the atoms that are the targets for the collisions. In a gas that has the same temperatures of ions, neutrals and electrons, all the particles have the same average kinetic energy so the electrons will have larger average velocities by a factor of $(\mathrm{m}_{atom}/\mathrm{m}_e)^{1/2}$. For this reason collisions between ions and electrons occur at a much higher rate than those between ions and neutrals, the latter usually negligible unless the gas is almost entirely neutral.

As an aside, it is possible for electrons and ions to have different temperatures. When electrons and ions encounter a shock wave with velocity v_S, some fraction of the incident kinetic energy $(\mathrm{m}/2)\mathrm{v}_S^2$ for each particle is converted to thermal energy kT. Because ions are heavier, their postshock temperatures

are correspondingly higher. Differences between ion and electron temperatures gradually equilibrate behind the shock, a process followed by all modern shock codes. The effect on line emission can be important, for example in supernova shells [28].

Single Ion Analysis: High and Low Density Limits, n_e and T_e

Equation 6 naturally separates densities into two regimes, depending on the electron density. In the low density limit (LDL), $n_e << n_C$ and collisional de-excitation is unimportant. In this limit every collisional excitation from the ground state to the upper state is followed by radiative decay and the emission of a photon. Alternatively, in the high density limit (HDL), $n_e >> n_C$, so most collisional excitations are followed by collisional de-excitations. In this case, the collisional de-excitations 'quench' excitations that would otherwise produce photons. As far as the dynamics of the gas is concerned, energy is only lost from the system (i.e., the gas cools) when photons escape the gas. Collisional excitations followed by collisional de-excitations do not cool the gas because the net effect is simply to transfer energy from one free electron (the one doing the excitation) to another free electron (the one doing the de-excitation).

We would like to determine which emission line ratios are useful for measuring temperature, electron density, and so on. Consider Figure 1, which shows two hypothetical three-level atoms A and B. Levels 2 and 3 in atom A have nearly the same excitation relative to ground, so the frequencies of the 2-1 and 3-1 transitions are nearly identical. From equations 1, 2, 3, and 6, the ratio of the line intensities I_{31}/I_{21} in the LDL simply equals C_{13}/C_{12}, the ratio that collisions from the ground populate these levels. This result makes sense because in the LDL, all collisional excitations produce a photon when the atom decays back to its ground state. As we shall see below, for closely-spaced energy levels the ratio C_{13}/C_{12} equals the ratio of collision strengths Ω_{13}/Ω_{12} between the respective levels. Collision strengths are independent of the electron density and usually nearly independent of the temperature, so the ratio of the line intensities is a fixed number in the LDL.

In the HDL, the intensity ratio I_{31}/I_{21} approaches a different value, $(C_{13}/C_{12})\times (A_{21}/A_{31})$. Thus, the line ratio I_{31}/I_{21} changes from one asymptotic value at low densities to a different value at high densities. When the value for the electron density lies between the LDL and HDL, the observed ratio provides an estimate of the electron density. The observed ratio gives an upper limit for the density when the gas is in the LDL and a lower limit when the gas is in the HDL.

In atom B, levels 2 and 3 are at quite different energies, E_2 and E_3 respectively, above ground. In this case, the ratio of the collision rate coefficients C_{13}/C_{12} equals $\Omega_{13}/\Omega_{12}\times$ exp(-(E_3-E_2)/kT), so there is now also a temperature dependence to the ratio. This result reflects the fact that more electrons have sufficient energy to excite the atom from the ground level to level 2 than

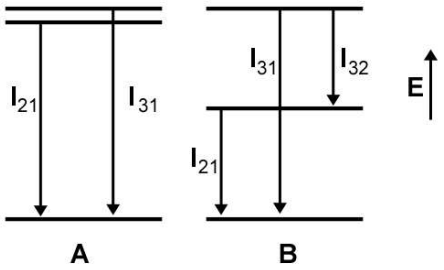

Fig. 1. Energy levels for two hypothetical atoms. The lower, intermediate, and upper levels are defined as levels 1, 2, and 3, respectively for both atoms.

are available to excite from the ground to level 3. In the HDL the temperature dependence remains, with the values modified by the factor A_{21}/A_{31} as for atom A. Hence, the emission line ratio I_{31}/I_{21} depends on both the electron density and on the temperature. Hence, the ratio of two line fluxes from an ion specifies a fixed curve in (n_e,T_e) space.

Another type of line ratio is one where the transitions share a common upper level, such as I_{32}/I_{31}. From equations 1 and 3 we see that this ratio simply equals $A_{32}\nu_{32}$ / $A_{31}\nu_{31}$. From a diagnostic standpoint this ratio would seem to be useless, as it is fixed regardless of the conditions in the plasma. There are, however, some uses for this type of line ratio. First, the ratio is a good check of the instrumental flux calibration when the emission lines are close in wavelength (i.e., the ground state is split; e.g. [N II] λ6583 / [N II] λ6548). In cases like Atom B in Fig. 1 where $\nu_{31} >> \nu_{32}$, one can use the observed line ratio to estimate the reddening (e.g. [S II] 1.03μm / [S II] λ4070, see Brugel et al. [5]). Alternatively, if one knows the reddening, it is possible to determine the ratio of the Einstein-A values of the transitions experimentally[48], which can then be used in other objects to find the reddening [34, 37].

In rare cases, line ratios from the same upper level may deviate from the ratio of the A-values when one of the transitions is permitted and goes to the ground level [21]. In these so-called resonance lines, the opacity (κ in equation 2) becomes large enough that some of the photons are absorbed by other atoms along the line of sight, which subsequently scatter the photons in a direction away from the observer, lowering their fluxes. This process only occurs with permitted lines, typically at ultraviolet wavelengths.

Multiple Ion Analysis: Ionization Fractions and Abundances

The analysis we have described thus far applies only to emission lines that originate from a single ion. Density and temperature dependencies of line ratios between different ions follow the same general guidelines described above, except that an observed line ratio is no longer just a function of the electron

temperature and density, but now also depends on the total abundance of each ionic species. If the same element is used (e.g. [N I] λ5200 / [N II] λ6583), then the ratio depends only on the ionization fraction of that element, while line ratios that mix elements (e.g. [O I] λ6300 / [S II] λ6731) also depend upon the ratios of the abundances of these elements.

To translate an observed electron density to a total density we need to know the ionization fraction of hydrogen, which is the dominant element. Fortunately, ionization fractions of N and O are tied closely to that of H through charge exchange (see below and Sect. 3), so one can usually obtain the ionization fraction of H in this manner.

Magnetic fields are particularly difficult to measure in stellar jets because the emission lines do not display any Zeeman splitting. It is possible to infer something about field strengths by studying shock waves. We will return to this issue in Sect. 4.

2.2 Physical Processes

Deriving the atomic physics relevant for studies of diffuse nebular gas is beyond the scope of this paper. However, it is useful to summarize the main results that come out of quantum mechanical studies of atoms, because this physics underlies the entire analysis of emission lines. In this section I provide such an outline, which is not intended to be a step-by-step derivation of all the physics. However, I have tried wherever feasible to not simply quote results, but instead highlight intermediate steps in the analysis so that the interested student may look for these in physics texts on the subject. There are several good references on atomic physics and line spectroscopy (e.g. [43, 2]).

Compilations of collision strengths, energy levels, A-values, charge exchange cross sections, photoionization cross sections, and photoexcitation cross sections for emission lines of interest exist in the literature [30]. The historical application of these processes to HH research is covered in Sect. 3.

Photoionization

Photoionization processes usually do not dominate the ionization balance within stellar jets. Unlike massive stars, T Tauri stars have relatively cool photospheres and do not emit substantial amounts of ionizing radiation. Some ionizing radiation does occur from hotspots where material falls onto the star, but this radiation is usually absorbed by the surrounding medium before it can propagate significantly into the jet. Ionization events do occur in stellar jets close to the source, but these do not appear to be caused by photoionization (see Sect. 4). However, photoionization is an important process in the cooling zones of shock waves, where, for example, Lyman continuum photons propagate both upstream and downstream of the shock front. These photons may either ionize preshock gas or re-ionize postshock gas.

The physics of photoionization comes down to calculating the photoionization cross section for the atom of interest as a function of frequency. Photoionization cross sections are zero up to an energy threshhold, where they jump to a peak value $a_\circ$ (cm^2), and then decline as the frequency increases. Above the threshhold, the photoionization cross section declines as $\nu^{-\alpha}$, where $\alpha \sim 3$ for H. Values for $a_\circ$ and α are tabulated in several references [36].

To describe photoionization quantitatively, note that in the presence of a magnetic field the momentum operator $\mathbf{p}$ becomes $\mathbf{p} + e\mathbf{A}/c$, where $\mathbf{A}$ is the magnetic vector potential. We can represent the effect the photon has on the Hamiltonian by using

$$\mathbf{A} = \mathbf{A}_\circ \cos(\mathbf{k} \bullet \mathbf{r} - \omega t) = \mathbf{A}_\circ \frac{e^{i(\mathbf{k}\bullet\mathbf{r}-\omega t)} + e^{-i(\mathbf{k}\bullet\mathbf{r}-\omega t)}}{2} \tag{8}$$

where $A_\circ$ is a constant. The momentum ($\mathbf{p} + e\mathbf{A}/c$) enters into the Hamiltonian as a squared term, and the photon may also interact with the atom via a $\mu_\mathbf{S} \bullet \mathbf{B}$ term, where $\mu_\mathbf{S}$ is the magnetic moment of the atom for spin S. Ignoring this spin term for the moment, and discarding the usually negligible e^2A^2/c^2 term that arises from squaring the momentum, we obtain an expression for the interaction terms H_{int} in the Hamiltonian that represent how the radiation affects the state of the atom,

$$H_{int} = \frac{e}{2mc} \left(\mathbf{p} \bullet \mathbf{A} + \mathbf{A} \bullet \mathbf{p}\right). \tag{9}$$

When, as in this case, the Hamiltonian can be written as the sum of an unperturbed component $H_\circ$ and a perturbation H_{int}, one can use perturbation theory to determine how an atom in an inital state $|\phi_1\rangle$ evolves with time. If the energy eigenstates of the atom are $|\phi_n>$ and the atom is in state 1 at t = 0, then the wavefunction at time t is

$$|\psi(t)>= \sum_n |\phi_n>< \phi_n|\psi(t)> . \tag{10}$$

Define $c_n(t) = < \phi_n|\psi(t) >$. Then the probability that the atom will be in state 2 at time t is given by

$$|< \phi_2|\psi(t)>|^2 = |c_2(t)|^2 . \tag{11}$$

To determine $c_2(t)$ we must perturb the Hamiltonian for some time interval T with an electromagnetic wave like that of equation 8. The result, which is not too difficult to show (e.g. [2]) is

$$c_2(t) = \frac{1}{i\hbar} \int_0^t e^{i\omega_{12}t'} H_{21}(t')dt' \tag{12}$$

where

$$H_{21} = \langle \phi_2|H_{int}|\phi_1\rangle \tag{13}$$

is the matrix element between the initial and final states. In this case, the initial state '1' is a bound level, while the final state '2' is unbound, so ϕ_2 is a continuum state (sine wave) that represents the free electron.

The result of this exercise for H-like wavefunctions is that the cross section a_ν (units are cm^2; the ν refers to a cross section at a particular frequency) is

$$a_\nu = \frac{64\pi^4 m e^{10} Z^4}{3^{3/2} c h^6 n^5} \frac{g_\nu}{\nu^3} \tag{14}$$

where n is the initial level (equals 1 for ionization from the ground state), and g_ν is a Gaunt factor ~ 1 that varies slowly with frequency. Hence, $a_\nu \sim \nu^{-3}$, as noted above. The above expression for a_ν appears complicated, but the cross section at the threshold for ionization from level 1 simplifies to a numerical constant $(64/3\sqrt{3})$ times the fine structure constant $e^2/\hbar c$ times $\pi r_\circ^2$, where $r_\circ$ is the Bohr radius.

There is an interesting physical reason why the photoionization cross section drops as ν increases. The dominant term in the interaction Hamiltonian is the electric dipole matrix element $\langle \phi_2 | er | \phi_1 \rangle$, which in position representation is an integral that looks like

$$\int \int \phi_2^*(r, \Omega) er \phi_1(r, \Omega) r^2 \; dr \; d\Omega. \tag{15}$$

The integrand for the radial portion is a product of three functions, r^3, $\phi_2^*(r,\Omega)$, which is a sine wave, and $\phi_1(r,\Omega) \sim re^{-r}$ for the ground state 1s wavefunction. Visualizing the product of these three functions, it is clear that if ϕ_2^* oscillates slowly then the integrand will retain the same sign over the entire interval of r where the product $r^4 e^{-r}$ differs significantly from zero. However, when ϕ_2^* oscillates rapidly compared to the rest of the integrand, then the integral tends to cancel and the final result is much lower. Hence, a rapidly oscillating ϕ_2^*, which corresponds to a highly energetic free electron and therefore an energetic photon of large ν, leads to a smaller photoionization cross section. For this reason the photoionization cross section drops with frequency.

Photoexcitation and Pumping

Like photoionization, photoexcitation is a secondary process in stellar jets. The only transitions affected by photoexcitation in a significant way are permitted transitions where the lower energy level is populated enough to make the transition optically thick. In these so-called resonant lines, photons can be scattered out of the beam and change the line ratios relative to non-resonant lines. This phenomenon has been observed in ultraviolet resonance transitions of [Fe II] in HH 47A with HST spectra [21].

Classically, one can calculate a photoexcitation cross section with a model where the electron is tied to a spring that has some natural resonant frequency $\omega_\circ$ and damping constant γ, and the electron is subject to a passing

electromagnetic wave of frequency ω. The oscillating electron, being accelerated, emits light, and the ratio of the radiated power to the incident flux gives the cross section at that frequency. Integrating over all frequencies, we find

$$\int_0^\infty a_\nu d\nu = \frac{\pi e^2}{mc} f \ \ \mathrm{cm}^2\ \mathrm{s}^{-1}, \tag{16}$$

where the oscillator strength f equals unity in the classical approximation.

The quantum calculation is more involved, but follows in an analogous manner to the one we outlined for photoionization in the previous section. As in that case, we envision the atom starting out in an intial state $|\phi_1>$, and seek to determine what the probability is that it will occupy the final state $|\phi_2>$ after some time t under the influence of the electromagnetic perturbation.

Let us begin by taking the perturbation to be a single plane wave of angular frequency ω represented by an oscillating vector potential as in equation 8. Taking the electric field and the vector potential to be in the z-direction and the magnetic field in the x-direction, the wave moves in the y-direction so $\mathbf{k} \bullet \mathbf{r}$ = ky. Expanding the exponential term in equation 8,

$$e^{iky} \sim 1 + iky + ... \sim 1 \tag{17}$$

we find that the matrix element

$$H_{21} = \langle \phi_2 | H_{int} | \phi_1 \rangle = \frac{eA(t)}{c} < \phi_2 | \frac{p_z}{m} | \phi_1 > . \tag{18}$$

This is an operator equation, so one uses commutation relations between p_z, z, and the unperturbed Hamiltonian $\mathrm{H}_\circ$ to obtain

$$p_z = \frac{m}{i\hbar} \left(z H_\circ - H_\circ z \right). \tag{19}$$

Substituting the expression for p_z into the expression for H_{21} and using $\mathrm{H}_\circ|\phi_1> = \mathrm{E}_1|\phi_1>$ and $\mathrm{H}_\circ|\phi_2> = \mathrm{E}_2|\phi_2>$ we get

$$H_{21}(t) = \frac{A(t)}{ic\hbar}(E_1 - E_2) \langle \phi_2 | ez | \phi_1 \rangle = \frac{A(t)\omega_{12}}{ic} \langle \phi_2 | ez | \phi_1 \rangle \tag{20}$$

Using equation 12 we obtain an expression for c_2(t),

$$c_2(t) = \frac{-A_\circ \omega_{12}}{2\hbar c} \langle \phi_2 | ez | \phi_1 \rangle \, I(t) \tag{21}$$

where

$$I(t) = \int_0^t e^{i(\omega_{12}+\omega)t'} + e^{i(\omega_{12}-\omega)t'} dt'. \tag{22}$$

The integral is easy to solve as

$$I(t) = i \left[\frac{1 + e^{i(\omega_{12}+\omega)t}}{\omega_{12}+\omega} + \frac{1 - e^{i(\omega_{12}-\omega)t}}{\omega_{12}-\omega} \right]. \tag{23}$$

The first term in equation 23 is small compared with the second term when $\omega \sim \omega_{12}$. Rewriting the second term as a sine,

$$I(t) = -e^{\frac{-i(\omega_{12}-\omega)t}{2}} \left[\frac{e^{\frac{i(\omega_{12}-\omega)t}{2}} - e^{\frac{-i(\omega_{12}-\omega)t}{2}}}{2i\left(\frac{\omega_{12}-\omega}{2}\right)} \right]. \tag{24}$$

Hence,

$$|c_2(t)|^2 = \frac{A_\circ^2 \omega_{12}^2}{4\hbar^2 c^2} |\langle \phi_2 | ez | \phi_1 \rangle|^2 \frac{\sin^2\left(\frac{\omega_{12}-\omega}{2}t\right)}{\left(\frac{\omega_{12}-\omega}{2}\right)^2} \tag{25}$$

The function $|c_2(t)|^2$ represents the probability that the atom is in state 2 at time t under the influence of a single plane wave with angular frequency ω. Equation 25 has a peak at $\omega = \omega_{12}$, and the peak value increases as t^2, while the width of the peak scales as t^{-1}. Integrating the function over all frequencies yields a result proportional to the time t. Hence a uniform distribution of electromagnetic waves across the entire absorption profile results in a constant rate of excitation. For this reason, the rate of excitation must be proportional to the specific mean intensity J_ν (erg $cm^{-2}s^{-1}str^{-1}Hz^{-1}$). Using contour integration in the complex plane, we find

$$\int_{-\infty}^{\infty} \frac{\sin^2\left(\frac{\omega_{12}-\omega}{2}t\right)}{\left(\frac{\omega_{12}-\omega}{2}\right)^2} d\omega = 2\int_{-\infty}^{\infty} \frac{\sin^2(xt)}{x^2} dx = 2\pi t. \tag{26}$$

In real situations there is not a single plane wave with a frequency ω, but rather an input spectrum with a range of frequencies. To solve this case, consider a perturbation that begins at t = 0 and extends to time t. With the dipole approximation (equation 17), the perturbation is defined by some electric field $E(t) = E_\circ \sin(\omega t)$, or equivalently $A(t) = A_\circ \cos(\omega t)$ where

$$E = -\frac{1}{c}\frac{\partial A}{\partial t}, \tag{27}$$

and

$$E_\circ = -\frac{\omega A_\circ}{c}. \tag{28}$$

Equation 12 has a term proportional to $e^{i\omega_{12}t}A(t)$ within the integrand. Taking A(t) = 0 outside the time interval for the pulse, we can extend the limits to $\pm\infty$. The integral then becomes the Fourier transform $\hat{A}$ of the vector potential,

$$\hat{A}(\omega) = \frac{1}{2\pi}\int_{-\infty}^{\infty} e^{i\omega t} A(t) dt. \tag{29}$$

Combining these results yields

$$|c_2(t)|^2 = \frac{4\pi^2\omega_{12}^2}{\hbar^2 c^2} |\langle\phi_2|ez|\phi_1\rangle|^2 \left|\hat{A}(\omega)\right|^2. \quad (30)$$

For isotropic radiation,

$$|\langle\phi_2|ez|\phi_1\rangle|^2 = \frac{|\langle\phi_2|er|\phi_1\rangle|^2}{3}, \quad (31)$$

so that

$$|c_2(t)|^2 = \frac{4\pi^2}{3\hbar^2} |\langle\phi_2|er|\phi_1\rangle|^2 \left|\hat{E}(\omega)\right|^2. \quad (32)$$

Finally, we must relate $\hat{E}(\omega)$ and the mean intensity J_ν (erg cm^{-2}s^{-1}Hz^{-1}str^{-1}). For isotropic radiation, the total energy flux F (erg cm^{-2}s^{-1}) in any given direction is

$$\int_0^\infty 4\pi J_\omega d\omega = F = \frac{c}{4\pi t}\int_0^t E^2(t')dt' = \int_0^\infty \frac{c\left|\hat{E}(\omega)\right|^2}{t} d\omega, \quad (33)$$

so that

$$J_\omega = \frac{c\left|\hat{E}(\omega)\right|^2}{4\pi t}, \quad (34)$$

where we have used the fact that E(t') = 0 except for 0 < t' < t, $\hat{E}(\omega) = \hat{E}(-\omega)$, and Parseval's theorem

$$\int_{-\infty}^{\infty} E^2(t)dt = 2\pi\int_{-\infty}^{\infty}\left|\hat{E}(\omega)\right|^2 d\omega. \quad (35)$$

Using $J_\nu d\nu = J_\omega d\omega$ with $\omega = 2\pi\nu$ we obtain

$$J_\nu = \frac{c\left|\hat{E}(\omega)\right|^2}{2t}, \quad (36)$$

and

$$|c_2(t)|^2 = \frac{8\pi^2 J_\nu t}{3\hbar c} |\langle\phi_2|er|\phi_1\rangle|^2. \quad (37)$$

The Einstein B_{12} value is related to J_ν and $c_2(t)$ through

$$\frac{d|c_2(t)|^2}{dt} = J_\nu B_{12} \quad (38)$$

Hence,

$$B_{12} = \frac{8\pi^2}{3\hbar^2 c} |\langle\phi_2|er|\phi_1\rangle|^2. \quad (39)$$

The above analysis used the simplest possible expansion of the vector potential in equation 8. Keeping higher-order terms is warranted if the electric dipole moment matrix element in equation 8 is zero, in which case one must also include the $\mu_{\mathbf{S}} \bullet \mathbf{B}$ term. Higher order terms in the expansion of equation 8 lead to electric quadrupole and magnetic dipole transitions (see below).

Radiative Decay

Radiative or spontaneous decay refers to a situation where an atom in an excited state emits a photon and decays to a lower energy state. We can use the expression for B_{12} in equation 39 to find the Einstein A-value (units s^{-1}). In LTE, the mean intensity is the Planck function, and the ratio of the level populations n_2/n_1 is given by equation 5. Statistical equilibrium implies

$$n_2 \left(A_{21} + B_{21} J_\nu\right) = n_1 B_{12} J_\nu. \tag{40}$$

Substituting the Planck function B_ν for the mean intensity J_ν, where

$$B_\nu = \frac{2h\nu^3}{c^2 \left(e^{h\nu/kT} - 1\right)} \tag{41}$$

we find

$$A_{21} = \frac{2g_1 h\nu^3}{g_2 c^2} B_{12} \tag{42}$$

and

$$B_{21} = \frac{g_1}{g_2} B_{12}. \tag{43}$$

Using equation 39 for B_{12}, we find

$$A_{21} = \frac{64\pi^4 \nu_{21}^3 g_1}{3g_2 hc^3} \left|\langle \phi_2 | er | \phi_1 \rangle\right|^2. \tag{44}$$

Although the preceding equations were derived assuming LTE, they consist of relationships between atomic parameters and so are valid outside of LTE as well. For example, the A-value simply represents the rate at which an atom in level 2 will decay to level 1. This rate does not depend upon the level populations of other atoms in the gas. Owing to the ν^3 dependence, A-values at infrared wavelengths are much lower than those in the optical and ultraviolet. At ultraviolet wavelengths, $A \sim 10^8\ s^{-1}$, while that same line in the far-infrared will have $A \sim 0.1$, even though it is still a permitted line.

The transitions described above have a nonzero electric dipole moment matrix element and are called permitted lines. When this matrix element is zero, there may be nonzero components to the electric quadrupole or magnetic dipole moments that contribute to make the A-value nonzero. These emission lines are called forbidden, and are denoted with brackets (e.g. [N II] λ6583). At

optical wavelengths, the A-values of forbidden lines are typically a factor of 10^5 (magnetic dipole) to 10^8 (electric quadrupole) smaller than those of permitted lines. Nevertheless, forbidden lines are extremely important for nebular gas because they dominate the cooling at typical nebular temperatures of $\sim 10^4$ K (1eV). At these temperatures, transitions that would produce permitted lines are a factor of ~ 10 higher in energy than kT, making the permitted lines very weak because the upper states are simply not populated.

Emission lines between states with different spins are not allowed in the L-S coupling approximation, but they do occur in nature. Such lines are known as semiforbidden, or intersystem lines and are denoted with a single bracket (e.g. [C III λ1909). Semiforbidden transitions like [C III λ1909 are useful because they have A-values intermediate between forbidden and permitted lines, and so have high critical densities, but remain optically thin in many cases. Selection rules for the various electric and magnetic multipole radiation components are well-documented in the literature [47].

Collisional Excitation

In collisional excitation, a free electron collides with an atom and raises the atom to a higher energy state. The electron emerges from the collision as a free particle with a corresponding lower kinetic energy. Quantum mechanically, this is a scattering process with the incident electron represented as a plane wave, while the exiting electron is a scattered spherical wave with some scattering amplitude and phase shift. It is convenient to define the cross section σ_{12} of such a reaction in terms of a collision strength Ω_{12}, impact velocity v and statistical weight g_1 of the lower level as

$$\sigma_{12} = \frac{\pi \hbar^2 \Omega_{12}}{m^2 v^2 g_1} \tag{45}$$

Collision strengths are dimensionless, typically of order unity, and have the property that $\Omega_{ij} = \Omega_{ji}$.

The cross section will be zero for incident electron energies that are too low to excite the transition. Often the behavior of the cross section can be quite complex near the threshold excitation of the transition, and may exhibit a variety of resonances [6]. These resonances typically disappear when the cross sections are integrated over a Maxwellian distribution of electron velocities, as one encounters in a thermal plasma. When integrated over a Maxwellian, collision strengths are nearly independent of the temperature for most collisions of electrons and ions. Collisional cross sections between electrons and neutral atoms typically vary with temperature roughly as T^α, with $0.5 < \alpha < 1$.

The rate coefficient C_{12} is given by $< \sigma_{12} v >$, where the brackets indicate an average over the distribution of impact velocities. For a Maxwellian, the equation for the rate coefficient becomes

$$C_{12} = \frac{8.63 \times 10^{-6} \Omega_{12}}{g_1 T_e^{1/2}} e^{-h\nu_{12}/kT_e} \ \ \mathrm{cm^3 s^{-1}} \tag{46}$$

Owing to the complexity of resonances, the large number of energy levels, and the need to include relativistic perturbations into the analysis, reliable collision strengths are not always available for all transitions of interest, especially for heavier ions such as Fe II and Fe III, though availability of these quantities continues to improve gradually with time.

Charge Exchange

An example of a charge exchange reaction is $H^+ + O \rightarrow H + O^+$. Let the rate coefficient of this reaction be κ_1. The reaction may also proceed in the opposite direction with rate coefficient κ_2. In steady state, where N_X indicates the number density of species X,

$$(N_{H^+} N_O)\, \kappa_1 = (N_H N_{O^+})\, \kappa_2 \tag{47}$$

During the collision, the atoms briefly form an unbound state of the molecule OH^+, which then decays to either $H^+ + O$ or to $H + O^+$. The ionization state of H is 13.60 eV and for O is 13.62 eV. Hence, relative to a ground state defined by neutral H + O, the state '1' of $H^+ + O$ has an excitation of $E_1 = 13.60$ eV, while state '2' of $H + O^+$ has an excitation of $E_2 = 13.62$ eV.

In LTE, the ratio of the populations of states 1 and 2 are given by the Boltzmann equation

$$\frac{N_1}{N_2} = \frac{N_{H^+} N_O}{N_H N_{O^+}} = \frac{\kappa_2}{\kappa_1} = \frac{g_1}{g_2} e^{-(E_1 - E_2)/(kT)} \tag{48}$$

where $g_1 = g(H^+)g(O)$, and $g_2 = g(H)g(O^+)$ are the statistical weights of states 1 and 2, respectively. For temperatures of interest ($\sim \ 10^4$ K), H is all in the ground state, which has g(H) = 2, and $g(H^+) = 1$. The ground state configuration of O^+ is ${}^4S_{3/2}$, which has a statistical weight $g(O^+) = (2*3/2)+1 = 4$. In neutral O, there is a triplet state near the ground, ${}^3P_{2,1,0}$, with a total statistical weight of (2*2)+1 + (2*1)+1 + (2*0)+1 = 9. Hence, $g_1 = 9$ and $g_2 = 8$. Putting this all together we have

$$\frac{N_{O^+}}{N_O} = \frac{8}{9} e^{-0.02eV/(kT)} \frac{N_{H^+}}{N_H} \tag{49}$$

Hence, if the charge exchange cross sections are large enough, this process will tie the ionization fractions of atoms together, weighted by their respective statistical weights and a Boltzmann factor that represents differences in the ionization states of the atoms. Because H atoms are so abundant and He is typically neutral, when charge exchange occurs it almost always involves H. Charge exchange cross sections are particularly large between H and O.

2.3 Isoelectronic Sequences

An isoelectronic sequence refers to a group of atoms and ions that have the same number of electrons. For example, the isoelectronic sequence of 6 electron systems, all of which have ground electronic states of $1s^2 2s^2 2p^2$, consists of C I, N II, O III, Fl IV, Ne V, and so on. For the purposes of spectroscopy, atoms and ions within an isoelectronic sequence have identical patterns of energy levels, with the different nuclear charges acting as a scale factor in the binding energies for the levels. The reason for this behavior is that electrons in an unfilled outer shell determine the bound excited states of atoms, and two identical groups of such electrons produce the same sets of energy levels. Electrons become more bound as the number of protons in the nucleus increases, so the transitions shift to shorter wavelengths for higher atomic numbers. For example, wavelengths for the transitions from $^1D_2$ to $^3P_2$ in atoms with $6e^-$ decrease steady from 9849Å in C I, to 6583Å in N II, to 5007Å in O III, to 3426Å in Ne V.

Energy levels of light atoms are described well by L-S coupling. Heavier elements may require J-J coupling, but these are rarely of any interest in nebular studies because their abundances are very low. In L-S coupling, energy levels are defined with a notation ^aX_b, where a = 2S + 1 is the multiplicity, with S a number representing the total spin, X is the letter S, P, D, F, ... corresponding to L = 0, 1, 2, 3, ... where L is the total orbital angular momentum, and b is the J-value, which ranges from L + S, L + S − 1, ... L − S. For two electrons, one calculates the range of L and S allowed within a particular shell by adding together the individual l_i and s_i ($s_i = 1/2$ for all electrons) in the shell by the rules $L = l_1 + l_2, l_1 + l_2 - 1, \ldots |l_1 - l_2|$, and $S = s_1 + s_2, s_1 + s_2 - 1, \ldots |s_1 - s_2|$. Rules for more than two active electrons have similar forms.

One complicating factor when the n-values for the electrons are the same, as occurs in the ground configuration, is that electrons are fermions, and cannot occupy identical quantum states. Electrons with the same n and l-values are called equivalent electrons, and calculating which levels are excluded on the basis of the Pauli principle can be somewhat involved.

As an example, consider the case of an atom that has all but two of its electrons in filled lower shells ($1s^2$, $2s^2$, etc.), with the two remaining electrons each in a p-shell. Here, $l_1 = l_2 = 1$ (p-states have l = 1), and $s_1 = s_2 = 1/2$ (electrons are spin 1/2 particles). Then L = 2, 1, or 0, and S = 1 or 0. As a result we expect three triplet states, $^3S_1$, $^3P_{2,1,0}$, $^3D_{3,2,1}$, and three singlet states, $^1S_0$, $^1P_1$, $^1D_2$. All of these states exist for two non-equivalent p-electrons, for example in the excited electronic state $1s^2 2s^2 2p3p$. However, when the electrons are equivalent, as in the ground electronic state $1s^2 2s^2 2p^2$, application of the Pauli exclusion principle shows that the ^3D, ^3S, and ^1P states do not exist (e.g. Appendix B of Eisberg & Resnick [12]).

Two isoelectronic sequences that differ only in the n-value of their outer shells also have the same pattern of energy levels. For example, ions and atoms

that are part of an isoelectronic sequence with 14 electrons, including Si I, P II, and S III, all have ground electronic states of $1s^2 2s^2 2p^6 3s^2 3p^2$, and so have the same pattern of lower levels as do atoms in the 6-electron isoelectronic sequence: a ground triplet state $^3P_{2,1,0}$, a singlet first-excited state $^1D_2$ and a singlet second-excited state $^1S_0$.

Energy levels for outer shells that are more than half-filled are easier to model by considering the equivalent configuration of the same shell with a number of holes equal to the capacity of the shell minus the number of electrons. For example, $1s^2 2s^2 2p^4$, the isoelectronic sequence of 8 electrons (O I, Fl II, Ne III, etc.), is the equivalent of two holes in the p-shell, which holds a maximum of six electrons. The energy levels produced by $2p^4$ are identical to those of $2p^2$, with the exception that the J-values within the ^3P state are reversed: the ground state in the triplet is now $^3P_2$ instead of $^3P_0$.

With the above considerations in mind, there are five common isoelectronic sequences for abundant light elements (Table 1). For higher-Z elements, once the d-shells become populated the energy level diagrams become very complex, particularly when the shell is about half-filled (e.g. Fe II, which is $3d^5$). Neutral noble gases (Ne, Ar) with a filled outer p-shell exhibit no emission lines of interest in the infrared, optical or near-UV.

Table 1. Ground Electronic State Configurations for Abundant Ions

Configuration	Examples	Electrons
s^1	H I, He II,	1
	Li I, C IV, N V, O VI	3
	Na I, Mg II, Al III, Si IV	11
	K I, Ca II, Ti IV	19
s^2	He I	2
	C III, N IV, O V	4
	Mg I, Al II, Si III	12
	Ca I, Ti III	20
p^1/p^5	C II, N III, O IV	5
	Si II, S IV, Fe XIV	13
	Ne II, Na III, Mg IV, Al V	9
	Ar II, K III, Ca IV, Fe X	17
p^2/p^4	C I, N II, O III, Ne V	6
	O I, Ne III, Na IV	8
	Si I, P II, S III, Ar V	14
	S I, Ar III, K IV, Ca V	16
p^3	N I, O II, Ne IV, Na V	7
	P I, S II, Cl III, Ar IV, K V	15

Representative energy level diagrams for each of the five common isoelectronic sequence types are shown in Figure 2. We now consider how we might use each of the five types to analyze physical conditions in diffuse gas.

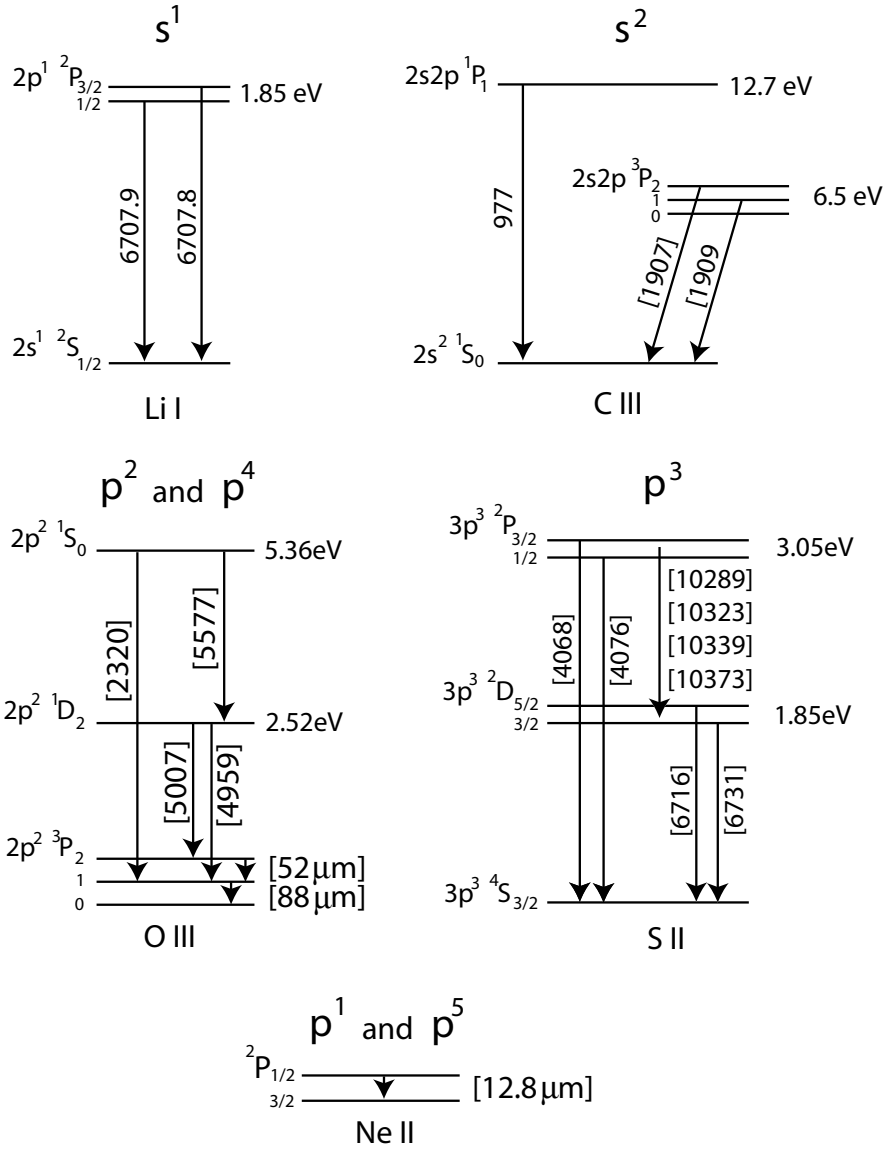

Fig. 2. Representative energy level diagrams for each of the five most common isoelectronic sequence types. Forbidden lines are denoted with two brackets, and semi-forbidden lines with a single bracket. Wavelengths are in Å unless otherwise noted, and are applicable only for the specific ion shown.

s^1: Permitted Resonance Lines

When a single electron lies in an outer s-shell, the atom is hydrogen-like, and the spectrum is dominated by permitted transitions between the various electronic excited states. Permitted transitions from the ground state are resonance lines that may be excited by photons. Because most of the atoms in a diffuse gas are in their ground states, these resonance transitions may become optically thick in HH objects.

In hydrogen, the first excited state lies 10.2 eV above ground, so the resonant lines are all in the ultraviolet as part of the Lyman series. However, atoms like Na I have a single electron in the 3s shell, which lies only about 2.1 eV below the 3p shell, so the transition falls in the optical as the Na D doublet at 5890Å and 5896Å. Likewise, the Li I resonance line so useful in establishing youth in T Tauri spectra comes from the 2p − 2s transition (Fig. 2), and is a closely-spaced red optical doublet at 6707Å. The resonance lines are all doublets because photons carry one unit of angular momentum, so the upper states of resonance absorption lines that originate from the ground s-shell must all be p-shells. A single electron in a p-shell is a doublet, with a spectroscopic configuration of $^2P_{3/2,1/2}$.

There are many well-known permitted resonance transitions of common s^1 elements, including C IV 1548+1550Å, N V 1243+1239Å, O VI 1032+1038Å, Na I 5890+5896Å (the "D" lines), Mg II 2796+2804Å, Al III 1855+1863Å, Si IV 1394+1403Å, and Ca II 3933+3968Å (the "K" and "H" lines, respectively). Many of these lines are seen in emission and in absorption in the spectra of active T Tauri star chromospheres, in classical T Tauri stars caused by accretion activity, and in the interstellar medium as narrow absorption features.

Ca II has an interesting complication in that the 3d energy level falls between the 4s and 4p levels responsible for the H and K lines. Transitions from 4p to 3d are allowed, and give rise to the 'infrared triplet' of emission lines at 8498+8542+8662Å that are bright in chromospherically active stars. The 3d state is metastable, and decays back to 4s via a pair of forbidden lines at 7291Å and 7324Å. Hence, unlike the majority of forbidden lines, the upper levels of these transitions may be pumped by photons under some circumstances. However, in HH objects the dominant means of excitation for the 3d state appears to be collisions [18]. The main use of the 7291Å line is to remove its companion line, 7324Å from a blend that includes the red quartet of auroral lines from O II, which are important as diagnostics of temperature, density and ionization fraction as described below.

The 2s state of H, which can be populated, for example, via an excitation from 1s − 3p followed by a decay 3p − 2s, is also a metastable state because an electron in the 2s level cannot decay to 1s by emitting a single photon without violating conservation of angular momentum. In a dense gas, collisions couple 2s to 2p, which can then decay to 1s, but in a low density gas like that found in HH objects ($n_e \sim 10^4$ cm^{-3}), the only viable way for the 2s state to decay to

1s is by emitting two photons, which is an allowed process if one includes the A^2 term in the perturbation expansion in equation 8. In 2-photon emission, a virtual energy level appears somewhere between 1s and 2s to facilitate the transitions. The virtual level can occur anywhere, so the resulting spectrum is a continuum that peaks in the ultraviolet around 1400Å [49].

Two-photon continua have been observed in HH spectra both in the blue and in the ultraviolet [7, 10]. The continua are strong because HH objects are mostly neutral and are excited by shock waves with enough energy to populate the n=2 level of hydrogen easily. The intrinsic spectral shape of the two-photon continuum is a fixed function that independent of physical parameters such as the density and the temperature, so one can easily infer the luminosity of the continuum by observing at a single wavelength and applying a bolometric correction [21].

s^2: Singlets, Triplets, and Semiforbidden Lines

Isoelectronic sequences with two electrons in an outer s-shell have two distinct sets of energy levels: a triplet state where the spins of the two electrons align, and a singlet state where the spins are antiparallel. Such systems are He-like, and have a ground state of $^1S_0$. The $^3S_1$ state does not exist for equivalent s-electrons owing to the exclusion principle, so the lowest energy triplet state is ^3P. Permitted (resonance) lines from higher singlet electronic states (e.g. $3s3p - 3s^2$) exist in the spectra, and permitted transitions also exist between the various triplet states.

For He I, the ground state $1s^2\ ^1S_0$ lies ~ 20 eV below the first-excited state, so transitions to ground are extreme ultraviolet or even soft X-ray photons. Transitions between the upper states give rise to many optical and infrared lines. For the singlets, these lines include $\lambda 2.058\mu$m (2p − 2s), $\lambda 5015$ (3p − 2s), and $\lambda 6678$ (3d − 2p). For the triplets, He I has $\lambda 10830$ (2p − 2s), $\lambda 3888$ (3p − 2s), and $\lambda 5876$ (3d − 2p). He I lines have been used recently by Edwards to probe the inner winds of jets [11].

Transitions also exist between the triplet states and the singlet states that may be either semiforbidden or forbidden. In the example depicted in Figure 2, the $\lambda 1909$ line of C III would be an electric dipole line were it not for the change of spin that makes it semiforbidden. The companion line at $\lambda 1907$ is forbidden (magnetic quadrupole) because the J-value changes by 2. The [C III $\lambda 1909$ line has been used to probe flows in young stars very close to the sources [14].

p^3: The Density Diagnostic

All p^3 configurations have a ground level and two well-spaced doublets as the upper levels (Figure 2). The capacity of the p-shell is 6 electrons, so a p^3 configuration is half-filled and there is no clear rule regarding which J-level has a higher energy within the doublets. For example, the $^2P_{3/2}$ state has a

higher energy than the $^2P_{1/2}$ state for N I, S II, and Ar IV, but a lower energy state for O II and Ne IV.

As we found in Sect. 2.1, flux ratios of the lines from upper-state doublets are density diagnostics. In the example in Figure 2, these include the [S II] 6716/6731 ratio, the [S II] 4068/4076 ratio and various combinations of the four infrared lines around 1μm. Ratios between transitions that originate from ^2P to those that start from ^2D are sensitive to both density and to temperature.

Unfortunately, the higher ionization p^3 configurations in Table 1 are usually not seen in HH jets, which have low ionization, and the [N I] 5198/5200Å ratio (the analog of [S II] 6716/6731) has a very low critical density and the lines are usually blended because they are so close together in wavelength. Hence, S II is the most important ion for density measurements, though O II is also useful when all the emission lines are bright enough to measure accurately.

p^2/p^4: Temperature and Reddening Diagnostics, Far-IR Lines

The p^2 and p^4 configurations are similar, each with a ^{3}P ground state, a first excited state of $^1D_2$ a few eV above ground, and a second excited state $^1S_0$ a few eV higher. Transitions between $^1D_2$ and ^3P are referred to as nebular lines, while transitions between $^1S_0$ and $^1D_2$ are auroral lines and those between $^1S_0$ and ^3P are transauroral lines. Auroral and transauroral lines are strong in the Earth's aurora because these lines have high critical densities; in contrast, nebular lines are bright in astrophysical nebulae where the densities are low enough to mitigate the effects of quenching. Ratios between nebular and auroral, and nebular and transauroral lines are good diagnostics of temperature, while ratios of auroral and transauroral lines give the reddening (Sect. 2.1).

Many of the brightest emission lines in HH objects come from this group of atoms, such as [C I] 9849+9823, [N II] 6548+6583, [O III] 4959+5007, [O I] 6300+6363, [O I] 5577, and [Ne III] 3869+3968. Forbidden transitions between the ^3P levels produce a number of well-known infrared lines, including [C I] 610μm, [N II] 204μm, [O I] 63μm, [O III] 88μm, and [Ne III] 15.4μm. In addition, the first excited electronic state (e.g. $2p^3 3s$ for the $2p^4$ atoms; $2s2p^3$ for $2s^2 2p^2$ atoms) gives a doublet level $^5S_{2,1}$ that generates a bright ultraviolet semiforbidden line in the transition to $^3P_1$. Examples include [O I 1302Å , [C I 2965Å , [N II 2140Å , and [O III 1663Å.

p^1/p^5: An Infrared Forbidden Line, and UV Permitted and Semiforbidden Lines

A single p-electron or hole has a single, closely-spaced doublet as a ground state, with $^2P_{1/2}$ level the lowest energy for p^1, and $^2P_{3/2}$ the lowest energy for p^5. Transitions within this doublet include [C II] 156μm, [N III] 57μm, [O IV] 26μm, [Si II] 35μm, [Ne II] 12.8μm, and [Ar II] 7.0μm, all in the infrared.

Highly ionized coronal lines of [Fe X] and [Fe XIV] are in the optical at 6375Å and 5303Å, respectively.

The first and second excited electronic states for p^1 and p^5 occur when an electron from the s-shell is excited to the p-shell. The resulting configuration has two p-electrons, and one s-electron hole. The result gives $p^2\ ^4P$ and $p^2\ ^2D$ states, which may decay to ground and give rise to both forbidden and semiforbidden transitions. Examples include [C II 2325Å and C II 1335Å.

3 Applying Nebular Line Diagnostics to Stellar Jets

Within the first decade after their discovery, Böhm [3] applied standard nebular diagnostic techniques to spectroscopic observations of the brightest HH object, HH 1. The analysis relied upon the ratio of nebular to auroral lines within O I and S II to constrain the temperature and the density. The results, which still hold today some 50 years hence, are that a typical electron temperature is $\sim$ 8000 K and typical electron density $\sim 10^4 \mathrm{cm}^{-3}$. The analysis also included line ratios between different elements, such as O and Ne.

The nature of the heating source of HH nebulae was a significant puzzle until the mid-70's. In his discovery paper, Herbig [26] noted the lack of nearby blue photoionizing stars near HH 1 and HH 2, which seemed to rule out photoionization as a heating source. However, not all HH objects were as isolated from stellar radiation, and in 1974, Strom et al. [50] found an extended emission line source HH 102 in the L 1551 star formation region that was also a reflection nebula. We now know that HH 102 is a rather unusual object, and contains a mixture of 'true' HH emission nebulae superposed upon an extended reflection nebula that marks the edge of an outflow cavity. Motivated by HH 102, Strom et al concluded that all HH objects were reflecting the light of a young star. The reflection nebula hypothesis was able to account for the mostly blueshifted radial velocities seen in HH objects, because circumstellar dust in an infalling envelope will see any emission lines from the star to be blueshifted, and will reflect that blueshifted line emission to the observer.

A few years later, Schwartz [45] came up with the modern explanation that shock waves excite HH objects. Schwartz was motivated by the similarity between HH spectra and those of supernova remnants, where a range of ionization states exist. In addition, the emission line analysis showed HH objects to have a low filling factor, as expected for the cooling zones of shocks. A few years later, Schwartz [46] found supersonic velocity dispersions of $>$ 100 $\mathrm{km\,s}^{-1}$ in HH objects, and noted that large line widths occur when a bow shock forms around a stationary obstacle in the flow. As the 1970's drew to a close, Schmidt and Miller [44] put the reflection nebula hypothesis to rest by noticing that while continuum in HH objects is polarized, emission lines are not, so the emission lines were intrinsic to the object and not scattered light.

The realization that HH objects were shock waves led to a great deal of theoretical work (e.g. by Raymond [41], and Dopita [9] with the goal of

explaining the observed emission-line ratios. With the advent of computers, it became possible to model the physical conditions within a cooling zone of a shock and to predict the line emission from such a zone. The computer revolution also greatly facilitated calculations of the collision strengths and A-values needed to address this problem. Shock models of HH objects enjoyed some success, but it was clear that no single shock model could reproduce the observations well.

The first comprehensive work on the emission-line analysis of HH objects is the classic 1981 paper of Brugel, Böhm, and Mannery [5]. This paper stands today as an outstanding analysis of emission lines in HH objects. By combining dozens of emission lines from various elements for several HH objects, the authors made several key discoveries, and pointed out some fundamental limitations as well. The new spectra reproduced the earlier measurements of T_e and N_e, but the uncertainties were low enough to show a real intrinsic scatter in the measurements, indicative of a range of temperatures and densities. These observations clearly showed that emission-line analyses are problematic when the cooling zones of the shock waves are not resolved spatially, because in that case a wide range of densities and temperatures contributes to the observed line ratios. Another important result was that the volume filling factors were typically 1% or less, implying a filamentary, clumpy emitting zone. The authors also attempted to determine the role of dust in the flows by measuring refractory abundances, but the uncertainties were high.

When Herbig and Jones [27] presented the first proper motion study of HH objects in 1981, it finally became clear that HH objects represented dense, bullet-like objects in highly collimated outflows. The collimated nature of the flows implied that redshifted flows were rare simply because they propagate into the dark cloud where the extinction is high. The combination of large emission line widths found by Hartmann and Raymond [25] and high-excitation lines of C IV discovered in the first ultraviolet observations of Böhm, Ortolani, and their collaborators [4, 35] gave further support to the notion of HH objects as bow shocks. Very good matches to position-velocity diagrams from long-slit spectra by Raga et al. [39] and to velocity-resolved integrated emission line profiles by Hartigan et al. [24] were possible by incorporating radiative shock models with a bow shock geometry, although the bow shocks were not affixed to stationary cloudlets as Schwartz envisioned, but rather resembled those that would accompany a bullet of dense gas that moved through the surrounding medium.

The availability of CCD's made deep emission line images possible, and one of the first discoveries from this work (Mundt and Fried [32]) was that HH objects are typically parts of dense jets. Hartigan [16] noted that one of the expectations for shocks in jets is that both a bow shock (in the medium ahead of the shock) and a Mach disk (in the jet) should occur, and that both shocks should be visible, and subsequent observations by Morse, Reipurth and their collaborators [31, 42] showed this to be the case from both emission line ratios and kinematics. It became clear from these studies that bow shocks in

jets typically move into the wakes of previous ejections, a notion published earlier by Dopita [8].

As described in Sect. 2, observations of emission line ratios from p^3 ions like S II give direct measures of the electron density, provided the gas is not in the HDL or LDL. To convert an electron density to a total density one needs to estimate the ionization fraction in the gas. The correction can be large because HH object jets are mostly neutral.

It is certainly convenient to think of the jet as being filled with some plasma of a fixed density and ionization fraction. However, it is important to realize that the ionization fraction, like the electron density, varies dramatically for shocked flows. As neutral material enters a shock, the temperature rises sharply to the postshock value, and collisions gradually ionize the atoms. While this process occurs, the gas radiates emission lines and cools. Shock models show that the ionization fraction peaks at some value and then gradually declines. Most forbidden emission lines occur in a region where the ionization fraction is declining, so the value that one measures for the ionization fraction depends on where the ions used for the measurement are located in the postshock flow. Using emission lines to constrain the shock models in their 1994 paper, Hartigan et al. [23] found the ionization fractions of the brightest portions of some famous jets to be only a few percent.

Instead of using shock models, one can try to infer physical conditions along the jet by simply using the observed emission line ratios everywhere in the flow, as was done for large apertures in the Brugel et al 1981 paper. This procedure is the equivalent of modeling the emitting gas as having a constant density, temperature, and ionization fraction over the aperture or pixel of the observed line ratios. As Brugel et al. showed in their paper, analyzing emission lines in this manner is of limited value for systems like HH 1 and HH 2, which are dense, high-shock-velocity objects with unresolved cooling zones whose emission lines span a wide range of ionization states. Similar issues were found by Podio et al. [38] who analyzed both infrared and optical emission lines.

However, there are cases where the cooling zones are resolved, for example in many HST images. For resolved images, a single density, temperature, and ionization state may characterize the gas well. For these cases, Bacciotti & Eislöffel [1] used an analysis similar to that of Brugel et al., but also used the fact that the charge exchange cross sections were large enough to effectively tie the ionization fractions of N and O to that of H as described in Sect. 2.2. By incorporating charge exchange into the analysis in this manner, one can use the bright red emission lines of [O I], [N II], and [S II] to infer all the physical properties of interest. Results from this analysis show the ionization fractions range from a few percent in the regions that overlap the Hartigan et al. study (and therefore are in agreement with those results), to tens of percent in other regions. Of particular interest was the result that some jets appear to have ionization fractions that decline as they move away from their sources, suggesting some heating event close to the source.

Even with good measures of ionization fraction and density, estimates of mass loss rates in jets are plagued with uncertainties caused by the inherent clumpy nature of the flows, as I discussed in a recent review [17]. Emission line fluxes increase with the density, so images emphasize dense regions that cool rapidly. There may be cool dense regions within the jet that do not radiate, as well as less dense material that fills a larger fraction of the volume within the jet. The best procedure is probably to measure the mass loss rate as close as possible to the star, before shock waves concentrate the jet into clumps. In any case, because jets are mostly neutral they carry a larger amount of energy and momentum than one would infer by simply using their electron densities, as was done in some early papers [33].

4 Some New Results, Future Prospects

When I presented this lecture in Elba, I included results from two papers that were in the process of being submitted to the Astrophysical Journal. These papers have now been accepted for publication, so I will summarize the results only briefly here.

4.1 Slitless Spectroscopy and a New Analysis Method for Emission-Line Objects

The first paper [22] uses the rather unusual technique of slitless spectroscopy. By opening the spectroscopic slit wide enough to include emission from the entire jet, one obtains an image for each emission line in the jet with a single exposure. The technique is limited to objects that are not resolved spectrally. Using HST over two epochs, we were able to obtain high signal-to-noise images of many emission lines.

Of particular interest to this review is the new analysis technique introduced in the paper, which can be employed for any emission line object. Rather than use a specific emission-line ratio to infer electron densities, another to estimate the temperature, and so on, the paper developes a method where one uses all the emission line ratios, appropriately weighted according to their uncertainties, of all the lines in the analysis. The advantage of this technique is particularly apparent close to the star, where the [S II] 6716/6731 ratio is in the HDL. In the new analysis, the ratio simply provides a lower limit to the density, as it should, and the actual density measurement is constrained more by ratios that involve higher critical density lines such as [O I] 6300. The optimal solution for the electron density, temperature, and ionization fraction are those that minimize a quadratic form that resembles a chi-square, although the statistical distribution is more complex because the line ratios are not necessarily independent of one another.

The analysis yields several intriguing maps of the physical parameters in the HH 30 jet. Since the data were taken in two epochs separated by two

years, it is possible to follow proper motions in the jet and observe how the physical parameters vary with time. Results include a drop of ionization with distance, an increase of density along the axis of the flow, and what appear to be heating events that ionize the flow within $\sim$ 100 AU of the source and move outward with the flow. By observing such phenomena we can begin to connect the dynamics of jets with the accretion disks that drive them.

4.2 Magnetic Fields in Jets

Magnetic fields are particularly difficult to constrain from emission line ratios because the lines do not show Zeeman splitting. However, one can estimate field strengths by knowing enough about the shock. For example, given the preshock density (constrained by the observed line fluxes), and shock velocity (determined by the line ratios and observed shape of the bow shock), a shock model predicts what the electron density should be in the cooling zone. Observed electron densities are at least an order of magnitude lower than the predicted value, indicative of some other source of pressure. Even a small magnetic field in the preshock gas translates into a significant pressure in the postshock region, and will lower the observed electron density there.

Results from this analysis by Morse and collaborators [31] are that magnetic fields in front of bow shocks in jets are low, $\sim 15\mu$G. Although one might expect magnetic fields to be strong in jets if they are driven by magnetized accretion disks, these observations indicate that fields play only a minor role in the dynamics at large distances. The only field measurement close to the source seems to be that of Ray et al. [40], who found strong fields of the order of a few Gauss at distances of tens of AU from the source.

Can we reconcile a jet being strongly magnetized at the source, but only weakly-magnetized at large distances? For a magnetized disk wind the field will be mostly toroidal at large distances, and will scale as r^{-1}, while the density drops as r^{-2} for a collimated jet. Hence $\mathrm{B} \sim \mathrm{n}^{0.5}$, so the magnetic signal speed should remain constant with distance and a flow that is strongly magnetized (e.g. $\mathrm{V}_{Alfven} \sim 100$ km s^{-1}) should remain so at large distances. In fact, such a strong field would prohibit any weak shocks from forming in the jet, but we know shock velocities in jets are ~ 30 km s^{-1} from proper-motion measurements as well as emission-line studies [23, 20].

In order to study this issue we performed the first pulsed magnetized simulations aimed at connecting physical conditions at large distances with those present near the source. The main results, to appear in print this year [19], show that $\mathrm{B} \sim \mathrm{n}$ in shocks and rarefactions, so the global structure of a pulsed jet follows some intermediate power $\alpha \sim 0.85$, where $\mathrm{B} \sim \mathrm{n}^{\alpha}$. Because $\alpha > 0.5$, the magnetic signal speed drops with distance, on average and the jet gradually becomes more hydrodynamic instead of MHD at larger distances from the source. Essentially the velocity perturbations sweep the field into a few dense magnetized blobs that are separated by low field regions.

4.3 Future Research

Future research of emission lines in HH objects and jets will probably divide scientifically into two broad categories. On the one hand, there is a great deal of interest in connecting the jets to their launching points in the accretion disks that surround young stars. The process of accretion and collimated outflow occurs elsewhere in the universe (interacting binaries, black holes, AGN's, and perhaps even planetary nebulae), but the phenomenon is easiest to study in young stars because HH jets radiate emission lines and are spatially resolved. Many unanswered questions remain in this area, including the role that magnetic fields play in driving the jet, the importance of time variability and instabilities, how mass is loaded from the disk into the jet, and the transfer of angular momentum from the disk to the outflow.

A second broad area is the study of the fluid dynamics within HH flows. Many questions remain here as well, especially with regard to the role magnetic fields play in the dynamics of colliding clumps, the efficiency of entrainment along the edges of jets and the physics of the shock waves that couple the atomic outflow with that of the molecular gas. It may even be possible to create laboratory analogs of astrophysical jets [29, 13]. Being able to create jets in a laboratory setting is an attractive prospect, especially if the setup allows one to control the strength and geometry of magnetic fields in a collimated supersonic flow.

I close with a plea to everyone working in this field to try to obtain time-resolved spectra and images of HH jets over many epochs. Only with such data sets will we be able to really compare motions and shock waves in real jets with their numerical and laboratory analogs. Time-resolved data are the only way to determine the degree to which accretion is tied to outflow. The connection between accretion and outflow is perhaps the most fundamental aspect of the jet phenomenon, but our understanding of it remains superficial.

References

1. Bacciotti, F., & Eislöffel, J.: A&A **342**, 717, (1999).
2. Bransden, B., & Joachain, C.: "Introduction to Quantum Mechanics" (New York:Wiley) (1989).
3. Böhm, K.-H.: ApJ **123**, 379 (1956).
4. Böhm, K.-H., Böhm-Vitense, E., & Brugel, E.: ApJ **245**, L113, (1981).
5. Brugel, E., Böhm, K.-H., & Mannery, E.: ApJS **47**, 117, (1981).
6. Chen, G. et al.: Phys. Rev. A **74**, 2709, (2006).
7. Curiel, S., Raymond, J., Wolfire, M., Hartigan, P., Morse, J., Schwartz, R., & Nisenson, P.: ApJ **453**, 322, (1995).
8. Dopita, A.: A&A **63**, 237, (1978).
9. Dopita, M.: ApJS **37**, 111, (1978).
10. Dopita, M., Binette, L., & Schwartz, R.: ApJ **261**, 183, (1982).
11. Edwards, S.: this volume, (2007).

12. Eisberg, R., & Resnick, R.: "Quantum Physics of Atoms, Molecules, Solids, Nuclei, and Particles", (New York:Wiley), (1974).
13. Foster, J. et al.: ApJ **634**, L77, (2005).
14. Gomez de Castro, A. & Verdugo, E.: ApJ **597**, 443, (2003).
15. Haro, G.: AJ **55**, 72, (1950).
16. Hartigan, P.: ApJ **339**, 987, (1989).
17. Hartigan, P.: ApSS **287**, 111, (2003).
18. Hartigan, P., Edwards, S., & Pierson, R.: ApJ **609**, 261, (2004).
19. Hartigan, P., Frank, A., Varniere, P., & Blackman, E.: ApJ in press, (2007).
20. Hartigan, P. Morse, J., Reipurth, B., Heathcote, S. & Bally, J.: ApJ **559**, L157, (2001).
21. Hartigan, P., Morse, J., Tumlinson, J., Raymond, J., & Heathcote, S.: ApJ **512**, 901, (1999).
22. Hartigan, P., & Morse, J.: ApJ in press, (2007).
23. Hartigan, P., Morse, J., & Raymond, J.: ApJ **436**, 125, (1994).
24. Hartigan, P., Raymond, J., & Hartmann, L.: ApJ **316**, 323, (1987).
25. Hartmann, L., & Raymond, J.: ApJ **276**, 560, (1984).
26. Herbig, G. H.: ApJ **113**, 697, (1951).
27. Herbig, G. H. & Jones, B.: AJ **86**, 1232 (1981).
28. Laming, J., Raymond, J., McLaughlin, B., & Blair, W.: ApJ **472**, 267, (1996).
29. Lebedev, S. et al.: ApJ **616**, 988, (2004).
30. Mendoza, C.: IAU Symp. 103, "Planetary Nebula", (Dordrecht:Reidel), p143, (1983).
31. Morse, J., Hartigan, P., Cecil, G., Raymond, J., & Heathcote, S.: ApJ **399**, 231, (1992).
32. Mundt, R., & Fried, J.: ApJ **274**, L83, (1983).
33. Mundt, R., Brugel, E., & Bührke, T.: ApJ **319**, 275, (1987).
34. Nisini, B., Caratti o Garatti, A., Giannini, T., & Lorenzetti, D.: A&A **393**, 1035, (2002).
35. Ortolani, S. & D'Ordorico, S.: A&A **83**, L8, (1980).
36. Osterbrock, D.: Astrophysics of Gaseous Nebulae and Active Galactic Nuclei, (Mill Valley:University Science Books), p37, (1989).
37. Pesenti, N., Dougados, C., Cabrit, S., O'Brien, D., Garcia, P., & Ferriera, J.: A&A **410**, 155, (2003).
38. Podio, L., Bacciotti, F., Nisini, B., Eislöffel, J., Massi, F., Giannini, T., & Ray, T.: A&A **456**, 189, (2006).
39. Raga, A., & Böhm, K.-H.: ApJ **308**, 829, (1986).
40. Ray, T., Muxlow, T., Axon, D., Brown, A., Corcoran, D., Dyson, J., & Mundt, R.: Nature **385**, 415, (1997).
41. Raymond, J.: ApJS **39**, 1, (1979).
42. Reipurth, B., & Heathcote, S.: A&A **257**, 693, (1992).
43. Rybicki, G., & Lightmann, A.: "Radiative Processes in Astrophysics", (New York:Wiley), (1979).
44. Schmidt, G. & Miller, J.: ApJ **234**, L191, (1979).
45. Schwartz, R.: ApJ **195**, 631, (1975).
46. Schwartz, R.: ApJ **223**, 884, (1975).
47. Shevelko, V.: "Atoms and Their Spectroscopic Properties", (Heidelberg:Springer-Verlag), p41, (1997).
48. Smith, N., & Hartigan, P.: ApJ **638**, 1045, (2006).
49. Spitzer, L., & Greenstein, J.: ApJ **114**, 407, (1951).
50. Strom, S., Grasdalen, G., & Strom, K.: ApJ **191**, 111, (1974).